Explicit Solution of the Time Domain Volume Integral Equation Using a Stable Predictor-Corrector Scheme

Ahmed Al-Jarro, *Member, IEEE*, Mohamed A. Salem, *Member, IEEE*, Hakan Bağcı, *Member, IEEE*, Trevor M. Benson, *Senior Member, IEEE*, Phillip Sewell, *Senior Member, IEEE*, and Ana Vukovic, *Member, IEEE*

***Abstract*—An explicit marching-on-in-time (MOT) scheme for solving the time domain volume integral equation is presented. The proposed method achieves its stability by employing, at each time step, a corrector scheme, which updates/corrects fields computed by the explicit predictor scheme. The proposed method is computationally more efficient when compared to the existing filtering techniques used for the stabilization of explicit MOT schemes. Numerical results presented in this paper demonstrate that the proposed method maintains its stability even when applied to the analysis of electromagnetic wave interactions with electrically large structures meshed using approximately half a million discretization elements.**

***Index Terms*—Electromagnetic transients, explicit scheme, marching-on-in-time, time-domain analysis, time-domain volume integral equation.**

I. Introduction

In recent years, much progress has been reported on the development of time-domain integral equation (TDIE) solvers for analyzing transient electromagnetic wave interactions on various types of scatterers and for various applications [1]–[34]. TDIEs are typically solved using marching-on-in-time (MOT) techniques [1]–[27], where at each time step, computation of retarded fields/potentials, which involve temporal and spatial convolutions of the Green function with the time history of fields/currents induced on scatterers, is required. This requirement renders MOT-TDIE solvers susceptible to late-time instabilities and significantly increases their computational complexity. Therefore, the recent research efforts on TDIE solvers have been focused on developing accurate and stable, yet efficient, MOT schemes. The efficiency of TDIE solvers has been significantly increased with the development of the plane wave time domain (PWTD) algorithm [9]–[12] and the (blocked) fast Fourier transform (FFT)-based schemes [19]–[24] aimed at accelerating the computation of spatial and temporal convolutions. Furthermore, the problem of late-time instability, which has historically prohibited the widespread use of TDIE solvers, has been alleviated through the development of spatial and/or temporal filtering techniques [3], [6], [7], [32]–[34], accurate temporal interpolation rules [8], [17], [18], implicit MOT schemes [2], [5], [8], and highly accurate (semi-) analytic integration techniques [13]–[16].

TDIEs can be classified as surface [1]–[3], [7], [8], [13] and volume [9], [10], [30]–[34] integral equations (SIEs and VIEs). Obviously, the choice of a particular integral equation type depends on the nature of the problem under analysis. For analysis of wave interactions with metallic [1]–[3], [7], [8] and piecewise inhomogeneous scatterers [13], TD-SIE solvers are more appropriate; whereas for analysis of wave interactions with (arbitrarily) inhomogeneous scatterers, TD-VIE solvers are more suitable [9], [10], [30]–[34].

Furthermore, TDIE solvers can be classified as explicit [1], [3], [28]–[34] or implicit [2], [5], [8] schemes. The majority of the TDIE solvers developed to this date employ implicit MOT schemes for they are proven more stable than their explicit counterparts. In the implicit schemes, field/current values at the current time step are yet unknown; hence, the retarded fields radiated by those are not known. Therefore, the computation of the field/current values at the current time step requires the inversion of a matrix, which is denoted by $\mathbf{Z}_0$ here. The entries of $\mathbf{Z}_0$ are the discretized retarded-field interactions between spatial discretization elements, which are within distance $c\Delta t$ of each other. Here, Δt is the time step and c is the wave speed. When Δt is small, which typically happens when the frequency of excitation is high, smaller number of elements satisfy this criteria. Thus, $\mathbf{Z}_0$ is sparse and can be inverted very efficiently using an iterative solver [21], [25]–[27]. However, when Δt gets larger, which typically happens when the frequency of excitation gets lower, the number of elements, which are within distance $c\Delta t$ of each other increases; hence $\mathbf{Z}_0$ becomes much denser and therefore computationally more expensive to invert [21]. Additionally, if $\mathbf{Z}_0$ results from the discretization of the time-domain surface electric field integral equation, it suffers from low-frequency breakdown; it becomes ill-conditioned as the frequency of excitation gets lower [25]–[27]. This prohibits its efficient inversion using an iterative solver unless a carefully

Manuscript received January 07, 2012; revised April 17, 2012; accepted May 30, 2012. Date of publication July 10, 2012; date of current version October 26, 2012. This work was supported in part by an Academic Excellence Alliance program award from the King Abdullah University of Science and Technology (KAUST) Global Collaborative Research under the title "Energy Efficient Photonic and Spintronic Devices."

A. Al-Jarro, M. Salem, and H. Bağcı are with the Division of Physical Sciences and Engineering, King Abdullah University of Science and Technology (KAUST), 4700 King Abdullah University of Science and Technology, Thuwal 23955-6900, Saudi Arabia (e-mail: ahmed.aljarro@kaust.edu.sa).

T. M. Benson, P. Sewell, and A. Vukovic are with the School of Electrical and Electronic Engineering, University of Nottingham, Nottingham NG7 2RD, U.K.

Color versions of one or more of the figures in this paper are available online at http://ieeexplore.ieee.org.

Digital Object Identifier 10.1109/TAP.2012.2207691

formulated and implemented preconditioner is used [25]–[27]. Implicit schemes have traditionally been used in conjunction with Galerkin-based spatial discretization techniques [2], [5], [8].

On the contrary, explicit MOT schemes result in a diagonal $\mathbf{Z}_0$; and therefore no matrix inversion is required for computing the unknown field/current values at the current time step. Explicit schemes are, however, obtained at the expense of tying Δt to the minimum spatial discretization size in a Courant–Friedrichs–Lewy (CFL) condition like manner [37]. This might render Δt unnecessarily small; and therefore can significantly reduce the efficiency of the resulting MOT scheme. Fortunately, this limitation may be alleviated by using adaptive meshing and multi-rate/localized time stepping techniques similar to those incorporated into finite element-based solvers [38], [39].

The majority of the explicit MOT schemes that have been developed so far have been used in conjunction with nodal spatial discretization schemes [28]–[34]. These schemes can be thought of as simplified Galerkin methods, where testing integration and source expansion are performed using a single nodal point located at the center of each spatial discretization element [28]–[34]. Compared to the full Galerkin methods, these schemes are easier to implement and the computation of the interaction matrices resulting from the discretized retarded field/potential integrals is considerably faster. The obvious disadvantage of these schemes is the reduced stability [32]–[34]. To date, the instability problem of the explicit schemes has been alleviated using low pass finite-impulse response (FIR) filtering techniques [33], [34]. However, application of these techniques comes with a considerably increased computational cost since they are integrated into the MOT scheme in the form of a constant group delay. Additionally, design of the appropriate FIR might be challenging when analyzing structures involving the more complex material properties.

In this paper, a TD-VIE solver, which employs a nodal spatial discretization scheme and an explicit MOT algorithm in the form of a predictor-corrector scheme, is proposed. The proposed method is built upon the work of [32]–[34]; however, instead of using FIR based techniques to stabilize the solution, it makes use of a corrector step to update/correct fields values computed explicitly at the predictor step at each time step. The proposed method has the following advantages over the conventional implicit schemes: i) It is fully explicit and does not require any matrix inversion. ii) It does not precompute nor store any discretized retarded field interactions before the time marching starts; as a result, it is memory efficient. iii) The use of nodal spatial discretization schemes makes the computation of these discretized interactions fast. Thus, their repeated computation during marching does not increase the computational time drastically. It should be emphasized here that, like the implicit schemes, the proposed predictor-corrector scheme stays stable while computing the late time solution; and it maintains its stability even when applied to the analysis of wave interactions with structures meshed using approximately one million spatial discretization elements.

The remainder of the paper is organized as follows. Section II, first, details the formulation of the TD-VIE. Thereafter, it describes the implemented spatial and temporal discretization schemes leading to the explicit MOT algorithm in the form of predictor-corrector updates. In Section III, the accuracy and stability of the proposed TD-VIE solver is demonstrated via its application to the analysis of electromagnetic scattering from a layered microsphere. Additionally, Section III demonstrates the applicability of the TD-VIE solver to the characterization of wave interactions on more complex structures: The proposed solver is used in the generation of backscattered diffraction patterns of a triangular ensemble of three microspheres [40] and characterization of an elongated photonic nanojet in the detection of a thin film layer [41], [42].

II. Formulation

A. Time-Domain Volume Integral Equation (TD-VIE)

Consider a scatterer comprised of inhomogeneous dielectric volumes, which reside in an infinite homogeneous (background) medium. Let V represent the total volume of the scatterer. Frequency independent relative permittivities of the scatterer and the background medium are denoted by $\varepsilon(\mathbf{r})$, $\mathbf{r} \in V$, and ε_b, respectively. The scatterer and the background medium are assumed nonmagnetic: $\mu(\mathbf{r}) = \mu_b = 1$, where $\mu(\mathbf{r})$ and μ_b are frequency independent relative permeabilities of the scatterer and the background medium, respectively. The wave speed in the background medium is given by $c_b = c_0/\sqrt{\varepsilon_b \mu_b}$, where $c_0 = 1/\sqrt{\varepsilon_0 \mu_0}$, ε_0, and μ_0 are the wave speed, permittivity, and permeability in free space, respectively. Let $\mathbf{E}^{\mathrm{inc}}(\mathbf{r}, t)$ represent an incident electric field that is vanishingly small for $\mathbf{r} \in V$ and $t \leq 0$ and temporally band-limited to $f_{\max}$. $\mathbf{E}^{\mathrm{inc}}(\mathbf{r}, t)$ excites the scatterer; in return the equivalent polarization current, $\mathbf{J}(\mathbf{r}, t)$, is induced in V. $\mathbf{J}(\mathbf{r}, t)$, $\mathbf{r} \in V$, generates the scattered electric field $\mathbf{E}^{\mathrm{sca}}(\mathbf{r}, t)$:

$$\mathbf{E}^{\mathrm{sca}}(\mathbf{r}, t) = \frac{\mu_0}{4\pi} \left[c_b^2 \nabla\nabla - \partial_t^2 \bar{\mathbf{I}} \right] \cdot \int_0^{t - R/c_b} dt' \int_V dv' \frac{\mathbf{J}(\mathbf{r}', t')}{R} \tag{1}$$

where $R = |\mathbf{r} - \mathbf{r}'|$ is the distance between the field point $\mathbf{r}$ and the source point $\mathbf{r}'$, ∂_t^2 represents the second-order partial derivative with respect to time, and $\bar{\mathbf{I}} = \hat{\mathbf{x}}\hat{\mathbf{x}} + \hat{\mathbf{y}}\hat{\mathbf{y}} + \hat{\mathbf{z}}\hat{\mathbf{z}}$ is the unit dyadic. The incident and scattered fields, $\mathbf{E}^{\mathrm{inc}}(\mathbf{r}, t)$ and $\mathbf{E}^{\mathrm{sca}}(\mathbf{r}, t)$, satisfy

$$\mathbf{E}(\mathbf{r}, t) = \mathbf{E}^{\mathrm{inc}}(\mathbf{r}, t) + \mathbf{E}^{\mathrm{sca}}(\mathbf{r}, t) \tag{2}$$

where $\mathbf{E}(\mathbf{r}, t)$ is the total electric field. The equivalent polarization current $\mathbf{J}(\mathbf{r}, t)$ in (1) can be expressed in terms of the total electric field $\mathbf{E}(\mathbf{r}, t)$:

$$\mathbf{J}(\mathbf{r}, t) = (\varepsilon(\mathbf{r}) - \varepsilon_b)\varepsilon_0 \partial_t \mathbf{E}(\mathbf{r}, t). \tag{3}$$

Inserting (3) into (1), one can express $\mathbf{E}^{\mathrm{sca}}(\mathbf{r}, t)$ in terms of $\mathbf{E}(\mathbf{r}, t)$:

$$\mathbf{E}^{\mathrm{sca}}(\mathbf{r}, t) = \frac{1}{4\pi\varepsilon_b} \left[\nabla\nabla - \frac{\partial_t^2}{c_b^2} \bar{\mathbf{I}} \right] \cdot \int_V dv' (\varepsilon(\mathbf{r}') - \varepsilon_b) \frac{\mathbf{E}\left(\mathbf{r}', t - \frac{R}{c_b}\right)}{R}. \tag{4}$$

Finally, inserting (4) into (2) for $\forall \mathbf{r} \in V$ yields

$$\mathbf{E}(\mathbf{r},t) = \mathbf{E}^{\text{inc}}(\mathbf{r},t) + \frac{1}{4\pi\varepsilon_b}\left[\nabla\nabla - \frac{\partial_t^2}{c_b^2}\bar{\mathbf{I}}\right] \cdot \int_V dv'(\varepsilon(\mathbf{r}') - \varepsilon_b)\frac{\mathbf{E}\left(\mathbf{r}', t - \frac{R}{c_b}\right)}{R}, \mathbf{r} \in V. \quad (5)$$

Equation (5) is a time domain volume integral equation (TD-VIE) in the unknown total electric field, $\mathbf{E}(\mathbf{r},t)$, $\mathbf{r} \in V$, $t > 0$. It should also be noted here that (5) is a special form of the Volterra integral equation [28].

Several comments about (5) and its derivation are in order: i) In (5), the domain of integration is V, where the equivalent polarization current $\mathbf{J}(\mathbf{r},t)$ is nonzero, i.e., $\varepsilon(\mathbf{r}) \neq \varepsilon_b$. This means that the spatial discretization should only be applied on V, which immediately results in a significant advantage over differential equation-based formulations where the whole problem space needs to be discretized. ii) The kernel of the integral implicitly contains the correct asymptotic behavior of the fields at infinity, $R \to \infty$. This means that the computation domain does not need to be artificially terminated using absorbing conditions or perfectly matched layers as required by differential equation-based formulations. iii) In (5), $t - R/c_b$ is termed the retarded time; the retarded field volume integral is in essence the temporal and spatial convolution of the time history of currents/fields induced in V with the Green function of the background medium. The temporal convolution is reduced to simple time retardation since the Green function of the non-dispersive, non-dissipative, homogeneous, and infinite background medium is given by $\delta[(t-t') - R/c_b]$, where $\delta[.]$ represents the impulse function. iv) Even though (5) involves second-order space and time derivatives, unlike differential-equation based formulations, propagation of the fields is "realized" via the use of the background medium Green function. As a result, the numerical solution of (5) is less susceptible to numerical phase dispersion when compared to the numerical solution of differential-equation based formulations. v) During the derivation of (5), the scatterer and the background medium are assumed isotropic, non-dissipative, non-dispersive, and non-magnetic. Nevertheless, extension of the formulation to include anistropic, dissipative, dispersive, and magnetic material properties is rather straightforward [10], [20], [28], [30], [31].

B. Discretization Scheme

Consider a spatial discretization, where cubic elements of dimension Δd are used to divide V into N_e elements and a uniform time discretization, where Δt and N_t represent the time step size and the total number of time steps. The unknown total electric field $\mathbf{E}(\mathbf{r},t)$, $\mathbf{r} \in V$, $t > 0$, is sampled at the centers of the cubic elements, at $\mathbf{r} = \mathbf{r}_i$, $i = 1, \ldots, N_e$, and at times $t = t_n = n\Delta t$, $n = 1, \ldots, N_t$. These samples are denoted by $\mathbf{E}(\mathbf{r}_i, t_n)$, $i = 1, \ldots, N_e$ and $n = 1, \ldots, N_t$. Note that $\mathbf{E}(\mathbf{r}_i, t_n)$ holds all samples of the field's three components. This discretization scheme assumes that the field values and $\varepsilon(\mathbf{r})$ are constant within each discretization element. Samples of $\varepsilon(\mathbf{r})$ at $\mathbf{r} = \mathbf{r}_i$ are denoted by $\varepsilon(\mathbf{r}_i)$, $i = 1, \ldots, N_e$.

Discretization of the scattered field term in the right-hand side of (5) makes use of the samples of the volume integral

$$\mathbf{F}^s(\mathbf{r},t) = \frac{1}{4\pi\varepsilon_b}\int_V dv'(\varepsilon(\mathbf{r}') - \varepsilon_b)\frac{\mathbf{E}\left(\mathbf{r}', t - \frac{R}{c_b}\right)}{R}. \quad (6)$$

The samples $\mathbf{F}^s(\mathbf{r}_i, t_n)$ are approximated as

$$\mathbf{F}^s(\mathbf{r}_i, t_n) = \mathbf{E}(\mathbf{r}_i, t_n)S(\mathbf{r}_i) + \mathbf{F}(\mathbf{r}_i, t_n) \quad (7)$$

for $i = 1, \ldots, N_e$ and $n = 1, \ldots, N_t$. The first term in the right-hand side of (7) represents the contribution to $\mathbf{F}^s(\mathbf{r}_i, t_n)$ from $\mathbf{E}(\mathbf{r},t)$ sampled at $\mathbf{r} = \mathbf{r}_i$, i.e., the self-term contribution. In this case,

$$S(\mathbf{r}_i) = \frac{\varepsilon(\mathbf{r}_i) - \varepsilon_b}{4\pi\varepsilon_b}\int_{V_i}\frac{dv'}{|\mathbf{r}_i - \mathbf{r}'|} \quad (8)$$

where V_i is the volume support of the i^{th} element. The volume integral in (8) is computed analytically as described in [44]. In (7), the samples $\mathbf{F}(\mathbf{r}_i, t_n)$ represent the contributions to $\mathbf{F}^s(\mathbf{r}_i, t_n)$ from $\mathbf{E}(\mathbf{r},t)$ sampled at $\mathbf{r} = \mathbf{r}_i$, $j \neq i$, i.e., the non-self-term contributions

$$\mathbf{F}(\mathbf{r}_i, t_n) = \sum_{j\in K}\frac{\Delta d^3(\varepsilon(\mathbf{r}_j) - \varepsilon_b)}{4\pi\varepsilon_b R_{ij}}\mathbf{E}\left(\mathbf{r}_j, t_n - \frac{R_{ij}}{c_b}\right)$$
$$K = \left\{j : t_n - \frac{R_{ij}}{c_b} > 0, j \neq i\right\} \quad (9)$$

where $R_{ij} = |\mathbf{r}_i - \mathbf{r}_j|$ is the distance between the field point $\mathbf{r}_i$ and source point $\mathbf{r}_j$. In the computation of the samples $\mathbf{F}(\mathbf{r}_i, t_n)$ in (7), whenever $t_n - R_{ij}/c_b$ is not an integer multiple of Δt, $\mathbf{E}(\mathbf{r}_j, t_n - R_{ij}/c_b)$ is approximated using linear interpolation:

$$\mathbf{E}\left(\mathbf{r}_j, t_n - \frac{R_{ij}}{c_b}\right) = (1 - \alpha_{ij})\mathbf{E}(\mathbf{r}_j, t_{n-m}) + \alpha_{ij}\mathbf{E}(\mathbf{r}_j, t_{n-(m-1)}) \quad (10)$$

where $\alpha_{ij} = (m\Delta t - R_{ij}/c_b)/\Delta t$, $m = \lfloor R_{ij}/(c_b\Delta t)\rfloor$, and $\lfloor x \rfloor$ gives the largest integer that is less than or equal to x. Inserting (10) into (9) yields the samples $\mathbf{F}(\mathbf{r}_i, t_n)$ in terms of samples $\mathbf{E}(\mathbf{r}_i, t_n)$:

$$\mathbf{F}(\mathbf{r}_i, t_n) = \sum_{j\in K}\frac{\Delta d^3(\varepsilon(\mathbf{r}_j) - \varepsilon_b)}{4\pi\varepsilon_b R_{ij}} \times [(1 - \alpha_{ij})\mathbf{E}(\mathbf{r}_j, t_{n-m}) + \alpha_{ij}\mathbf{E}(\mathbf{r}_j, t_{n-m+1})]$$
$$K = \left\{j : t_n - \frac{R_{ij}}{c_b} > 0, j \neq i\right\} \quad (11)$$

for $i = 1, \ldots, N_e$ and $n = 1, \ldots, N_t$.

In the discretization of the spatial and temporal differential operators in the right-hand side of (5), the samples $\mathbf{F}^s(\mathbf{r}_i, t_n)$, given by (7), are then used. The samples of the term with the temporal derivative operator, which is given by

$$\mathbf{T}^s(\mathbf{r},t) = \frac{1}{4\pi\varepsilon_b}\frac{\partial_t^2}{c_b^2}\int_V dv'(\varepsilon(\mathbf{r}') - \varepsilon_b)\frac{\mathbf{E}\left(\mathbf{r}', t - \frac{R}{c_b}\right)}{R} \quad (12)$$

in the right-hand side of (5), $\mathbf{T}^s(\mathbf{r}_i, t_n)$, are approximated as

$$\mathbf{T}^s(\mathbf{r}_i, t_n) = \frac{\mathbf{E}(\mathbf{r}_i, t_n) - 2\mathbf{E}(\mathbf{r}_i, t_{n-1}) + \mathbf{E}(\mathbf{r}_i, t_{n-2})}{\Delta t^2}S(\mathbf{r}_i) + \mathbf{T}(\mathbf{r}_i, t_n) \quad (13)$$

for $i = 1, \ldots, N_e$ and $n = 1, \ldots, N_t$. The first term in the right-hand side of (13) is obtained by applying a backward difference (BD) scheme (see Appendix) to the samples of the self-term contribution in (7). On the other hand, the samples $\mathbf{T}(\mathbf{r}_i, t_n)$ in the right-hand side of (13), are approximated using either a CD (see Appendix) or a BD scheme that is applied on the samples $\mathbf{F}^s(\mathbf{r}_i, t_n)$ in (7) as described next.

Computation of $\mathbf{T}(\mathbf{r}_i, t_n)$ using CD applied on samples $\mathbf{F}^s(\mathbf{r}_i, t_n)$ requires the knowledge of $\mathbf{F}^s(\mathbf{r}_i, t_{n+1})$. A closer look at expressions of the samples $\mathbf{F}(\mathbf{r}_i, t_n)$ in (11) reveals that to compute $\mathbf{F}(\mathbf{r}_i, t_{n+1})$ [and hence $\mathbf{F}^s(\mathbf{r}_i, t_{n+1})$], one needs to know samples $\mathbf{E}(\mathbf{r}_j, t_{n-m+2})$. Note that, due to causality, at time step n, only samples $\mathbf{E}(\mathbf{r}_i, t_k)$, $i = 1, \ldots, N_e$, $k = 1, \ldots, n-1$ are known. This means that, for $m < 2$, $\mathbf{E}(\mathbf{r}_j, t_{n-m+2})$ are not yet known. The condition $m < 2$ is equivalent to the condition $R_{ij} < 2c_b\Delta t$; which means that for a given $\mathbf{r}_i$, CD cannot be applied to the terms of the summation in (11), which satisfy $|\mathbf{r}_i - \mathbf{r}_j| < 2c_b\Delta t$. For those terms, BD is used instead. In the light of this discussion, the samples $\mathbf{T}(\mathbf{r}_i, t_n)$ are expressed as

$$\mathbf{T}(\mathbf{r}_i, t_n) = \mathbf{T}^{BDR}(\mathbf{r}_i, t_n) + \mathbf{T}^{CDR}(\mathbf{r}_i, t_n) \tag{14}$$

where

$$\begin{aligned}\mathbf{T}^{BDR}(\mathbf{r}_i, t_n) &= \sum_{j\in BDR} \frac{\Delta d^3(\varepsilon(\mathbf{r}_j) - \varepsilon_b)}{4\pi\varepsilon_b R_{ij}\Delta t^2 c_b^2}[\alpha_{ij}\mathbf{E}(\mathbf{r}_j, t_{n-m+1}) \\ &\quad + (1-3\alpha_{ij})\mathbf{E}(r_j, t_{n-m}) + (3\alpha_{ij}-2)\mathbf{E}(r_j, t_{n-m-1}) \\ &\quad + (1-\alpha_{ij})\mathbf{E}(r_j, t_{n-m-2})] \\ \mathrm{BDR} &= \left\{ j : t_n - \frac{R_{ij}}{c_b} > 0, R_{ij} < 2c_b\Delta t, j \neq i \right\}\end{aligned} \tag{14a}$$

and

$$\begin{aligned}\mathbf{T}^{CDR}(\mathbf{r}_i, t_n) &= \sum_{j\in CDR} \frac{\Delta d^3(\varepsilon(\mathbf{r}_j) - \varepsilon_b)}{4\pi\varepsilon_b R_{ij}\Delta t^2 c_b^2}[\alpha_{ij}\mathbf{E}(\mathbf{r}_j, t_{n-m+2}) \\ &\quad + (1-3\alpha_{ij})\mathbf{E}(r_j, t_{n-m+1}) + (3\alpha_{ij}-2)\mathbf{E}(r_j, t_{n-m}) \\ &\quad + (1-\alpha_{ij})\mathbf{E}(r_j, t_{n-m-1})] \\ \mathrm{CDR} &= \left\{ j : t_n - \frac{R_{ij}}{c_b} > 0, R_{ij} \geq 2c_b\Delta t, j \neq i \right\}\end{aligned} \tag{14b}$$

where "BDR" and "CDR" represent the regions where BD and CD schemes are applied, respectively.

Samples of the term with the spatial differential operator, which is given by

$$\mathbf{L}^s(\mathbf{r}, t) = \frac{1}{4\pi\varepsilon_b}\nabla\nabla\cdot\int_V dv'(\varepsilon(\mathbf{r}') - \varepsilon_b)\frac{\mathbf{E}\left(\mathbf{r}', t - \frac{R}{c_b}\right)}{R} \tag{15}$$

in the right-hand side of (5), $\mathbf{L}^s(\mathbf{r}_i, t_n)$, are approximated as

$$\mathbf{L}^s(\mathbf{r}_i, t_n) = \bar{\mathbf{D}}(\mathbf{r}_i)\cdot\mathbf{E}(\mathbf{r}_i, t_n) + \mathbf{L}(\mathbf{r}_i, t_n) \tag{16}$$

for $i = 1, \ldots, N_e$ and $n = 1, \ldots, N_t$. The first term in the right-hand side of (16) represents the contribution to $\mathbf{L}^s(\mathbf{r}_i, t_n)$ from $\mathbf{E}(\mathbf{r}, t)$ sampled at $\mathbf{r} = \mathbf{r}_i$, i.e., the self-term contribution. In this case,

$$\bar{\mathbf{D}}(\mathbf{r}_i) = \frac{\varepsilon(\mathbf{r}_i) - \varepsilon_b}{4\pi\varepsilon_b}\int_{V_i}\nabla'\nabla'\frac{dv'}{|\mathbf{r}_i - \mathbf{r}'|} \tag{17}$$

where the volume integral is computed analytically as described in [45]. In (16), the samples $\mathbf{L}(\mathbf{r}_i, t_n)$ represent the contributions to $\mathbf{L}^s(\mathbf{r}_i, t_n)$ from $\mathbf{E}(\mathbf{r}, t)$ sampled at $\mathbf{r} = \mathbf{r}_j$, $j \neq i$, i.e., the non-self-term contributions; and are computed using central difference (CD) (see the Appendix) applied to the samples $\mathbf{F}^s(\mathbf{r}_i, t_n)$. In finite difference implementations, where possible, the space derivative is approximated at the middle point of the time derivative's approximation for increased stability [46]. Note that samples $\mathbf{T}(\mathbf{r}_i, t_n)$ (time derivative approximations) are computed using two methods, CD or BD schemes, depending on the proximity of the source point $\mathbf{r}_j$ to the field point $\mathbf{r}_i$ [see (14)]. Therefore, space derivative approximations, i.e., the samples $\mathbf{L}(\mathbf{r}_i, t_n)$, are computed accordingly in two parts:

$$\mathbf{L}(\mathbf{r}_i, t_n) = \mathbf{L}^{BDR}(\mathbf{r}_i, t_n) + \mathbf{L}^{CDR}(\mathbf{r}_i, t_n) \tag{18}$$

where

$$\begin{aligned}\mathbf{L}^{BDR}(\mathbf{r}_i, t_n) &= \bar{\mathbf{G}}_i\cdot\sum_{j\in BDR}\frac{\Delta d^3(\varepsilon(\mathbf{r}_j) - \varepsilon_b)}{4\pi\varepsilon_b R_{ij}} \\ &\quad\times[(1-\alpha_{ij})\mathbf{E}(\mathbf{r}_j, t_{n-m-1}) + \alpha_{ij_j}\mathbf{E}(\mathbf{r}_j, t_{n-m})]\end{aligned} \tag{18a}$$

and

$$\begin{aligned}\mathbf{L}^{CDR}(\mathbf{r}_i, t_n) &= \bar{\mathbf{G}}_i\cdot\sum_{j\in CDR}\frac{\Delta d^3(\varepsilon(\mathbf{r}_j) - \varepsilon_b)}{4\pi\varepsilon_b R_{ij}} \\ &\quad\times[(1-\alpha_{ij})\mathbf{E}(\mathbf{r}_j, t_{n-m}) + \alpha_{ij}\mathbf{E}(\mathbf{r}_j, t_{n-m+1})]\end{aligned} \tag{18b}$$

and the 3×3 matrix multiplication "$\bar{\mathbf{G}}_i\cdot$" approximates "$\nabla\nabla\cdot$", which is evaluated at $\mathbf{r} = \mathbf{r}_i$, using CD (see the Appendix), and "BDR" and "CDR" represent the regions where BD and CD schemes are applied to the time derivative, respectively [see (14a) and (14b)].

Inserting (13) and (16) into (5) and reorganizing the terms in the resulting equation yields

$$\begin{aligned}\mathbf{E}(\mathbf{r}_i, t_n) = \bar{\mathbf{M}}^{-1}\cdot\{&Q[2\mathbf{E}(\mathbf{r}_i, t_{n-1}) - \mathbf{E}(\mathbf{r}_i, t_{n-2})] \\ &+\mathbf{E}^{\mathrm{inc}}(\mathbf{r}_i, t_n) + [\mathbf{T}(\mathbf{r}_i, t_n) + \mathbf{L}(\mathbf{r}_i, t_n)]\}\end{aligned} \tag{19}$$

for $i = 1, \ldots, N_e$ and $n = 1, \ldots, N_t$. In (19), $\mathbf{E}^{\mathrm{inc}}(\mathbf{r}_i, t_n)$ are samples of the incident field $\mathbf{E}^{\mathrm{inc}}(\mathbf{r}, t)$; and

$$\bar{\mathbf{M}} = [1+Q]\bar{\mathbf{I}} - \bar{\mathbf{D}}(\mathbf{r}_i) \tag{19a}$$

and

$$Q = \frac{S(\mathbf{r}_i)}{c_b^2\Delta t^2} \tag{19b}$$

are a 3×3 matrix and a scalar, respectively. Equation (19) constitutes an explicit MOT scheme for computing samples $\mathbf{E}(\mathbf{r}_i, t_n)$, $i = 1, \ldots, N_e$ and $n = 1, \ldots, N_t$, provided that

$\Delta t \leq \Delta d/c_b$. Note that, under this condition, a closer look at (14a), (14b), A1, and (18b) reveals that $\mathbf{f}(\mathbf{r}_i, t_n)$ receives contributions only from samples $\mathbf{E}(\mathbf{r}_i, t_k)$, $i = 1, \ldots, N_e$, $k = 1, \ldots, n-1$. It should be noted here that Q and $\bar{\mathbf{M}}^{-1}$ are computed only once before time marching since $S(\mathbf{r}_i)$ and $\bar{\mathbf{D}}(\mathbf{r}_i)$ have the same value of for all discretization elements. Explicit schemes of this type are known to be unstable; previously FIR techniques have been used to alleviate the late time instabilities [34]; however, they increase the computational cost of the MOT scheme considerably. In the next section, a predictor-corrector scheme is proposed for stabilizing the MOT scheme (19) while maintaining its explicitness without increasing the computational cost.

C. Predictor–Corrector Scheme

The predictor step of the scheme is the same as the explicit MOT update presented in (19); the predictor update at time step n is given by

$$\mathbf{E}(\mathbf{r}_i, t_n) = \bar{\mathbf{M}}^{-1} \cdot \{Q[2\mathbf{E}(\mathbf{r}_i, t_{n-1}) - \mathbf{E}(\mathbf{r}_i, t_{n-2})] + \mathbf{E}^{\text{inc}}(\mathbf{r}_i, t_n) + [\mathbf{T}(\mathbf{r}_i, t_n) + \mathbf{L}(\mathbf{r}_i, t_n)]\} \quad (20)$$

for $i = 1, \ldots, N_e$. After the predictor update, in preparation for the corrector step, since $\mathbf{E}(\mathbf{r}_i, t_n)$, $i = 1, \ldots, N_e$, are now predicted and hence "known," one can use CD to compute $\mathbf{T}(\mathbf{r}_i, t_n)$ [see (14)] for all source and field point pairs, $\mathbf{r}_j$ and $\mathbf{r}_i$, $i = 1, \ldots, N_e$, $j = 1, \ldots, N_e$. This is achieved by updating only the contributions to $\mathbf{T}(\mathbf{r}_i, t_n)$ from $\mathbf{E}(\mathbf{r}_j, t_n)$ for all $\mathbf{r}_j$ satisfying $|\mathbf{r}_i - \mathbf{r}_j| < 2c_b\Delta t$ (i.e., reevaluating contributions from the BDR, see (14), using CD scheme), such that

$$\mathbf{T}(\mathbf{r}_i, t_n) = \tilde{\mathbf{T}}^{CDR}(\mathbf{r}_i, t_n) + \mathbf{T}^{CDR}(\mathbf{r}_i, t_n) \quad (21)$$

for $i = 1, \ldots, N_e$. Here, $\mathbf{T}^{CDR}(\mathbf{r}_i, t_n)$ is given by (14b) and

$$\tilde{\mathbf{T}}^{CDR}(\mathbf{r}_i, t_n) = \sum_{j \in BDR} \frac{\Delta d^3(\varepsilon(\mathbf{r}_j) - \varepsilon_b)}{4\pi\varepsilon_b R_{ij}\Delta t^2 c_b^2} [\alpha_{ij}\mathbf{E}(\mathbf{r}_j, t_{n-m+2}) + (1 - 3\alpha_{ij})\mathbf{E}(r_j, t_{n-m+1}) + (3\alpha_{ij} - 2)\mathbf{E}(r_j, t_{n-m}) + (1 - \alpha_{ij})\mathbf{E}(r_j, t_{n-m-1})]. \quad (21a)$$

Note that the samples $\mathbf{T}^{CDR}(\mathbf{r}_i, t_n)$ do not need to be recomputed after the predictor step; update of the samples $\mathbf{T}(\mathbf{r}_i, t_n)$ requires computation of only the samples $\tilde{\mathbf{T}}^{CDR}(\mathbf{r}_i, t_n)$, which are localized to all source and field point pairs, $\mathbf{r}_j$ and $\mathbf{r}_i$ satisfying $|\mathbf{r}_i - \mathbf{r}_j| < 2c_b\Delta t$. Similarly, the samples $\mathbf{L}(\mathbf{r}_i, t_n)$ are also updated from $\mathbf{E}(\mathbf{r}_j, t_n)$ for all $\mathbf{r}_j$ satisfying $|\mathbf{r}_i - \mathbf{r}_j| < 2c_b\Delta t$ using

$$\mathbf{L}(\mathbf{r}_i, t_n) = \tilde{\mathbf{L}}^{CDR}(\mathbf{r}_i, t_n) + \mathbf{L}^{CDR}(\mathbf{r}_i, t_n) \quad (22)$$

for $i = 1, \ldots, N_e$. Here, $\mathbf{L}^{CDR}(\mathbf{r}_i, t_n)$ is given by (18b) and

$$\tilde{\mathbf{L}}^{CDR}(\mathbf{r}_i, t_n) = \bar{\mathbf{G}}_i \cdot \sum_{j \in BDR} \frac{\Delta d^3(\varepsilon(\mathbf{r}_j) - \varepsilon_b)}{4\pi\varepsilon_b R_{ij}} \times [(1 - \alpha_{ij})\mathbf{E}(\mathbf{r}_j, t_{n-m}) + \alpha_{ij}\mathbf{E}(\mathbf{r}_j, t_{n-m+1})]. \quad (22a)$$

Finally, the corrector step is executed as

$$\mathbf{E}(\mathbf{r}_i, t_n) = \mathbf{M}^{-1} \cdot \{Q[2\mathbf{E}(\mathbf{r}_i, t_{n-1}) - \mathbf{E}(\mathbf{r}_i, t_{n-2})] + \mathbf{E}^{\text{inc}}(\mathbf{r}_i, t_n) + 0.5[\mathbf{T}(\mathbf{r}_i, t_n) + \mathbf{T}(\mathbf{r}_i, t_{n-1}) + \mathbf{L}(\mathbf{r}_i, t_n) + \mathbf{L}(\mathbf{r}_i, t_{n-1})]\} \quad (23)$$

for $i = 1, \ldots, N_e$. After the corrector step $\tilde{\mathbf{T}}^{CDR}(\mathbf{r}_i, t_n)$ and $\tilde{\mathbf{L}}^{CDR}(\mathbf{r}_i, t_n)$ are updated from the 'corrected' values of $\mathbf{E}(\mathbf{r}_i, t_n)$, $i = 1, \ldots, N_e$ using (21a) and (22a) respectively; then $\mathbf{T}(\mathbf{r}_i, t_n)$ and $\mathbf{L}(\mathbf{r}_i, t_n)$ are updated using (21) and (22) from "corrected" values of $\tilde{\mathbf{T}}^{CDR}(\mathbf{r}_i, t_n)$ and $\tilde{\mathbf{L}}^{CDR}(\mathbf{r}_i, t_n)$ respectively. It should be emphasized here again that these updates are local to source and field points satisfying $|\mathbf{r}_i - \mathbf{r}_j| < 2c_b\Delta t$. Equations (20) and (23) constitute the predictor-corrector pair at a given time step n, $n = 1, \ldots, N_t$.

Several comments about the above MOT algorithm "enhanced" with predictor-corrector updates are in order. i) The MOT scheme is still explicit and the restriction on the time step, $\Delta t \leq \Delta d/c_b$, is alleviated. The method produces practically stable solutions using Δt up to $\sim 1.5\Delta d/c_b$, as shown by the numerical results presented in the next section. ii) The total computational cost of the corrector steps during marching is $O(N_t N_e)$ since each corrector step requires only local updates. This computational cost is negligible when compared to that of the overall MOT scheme, which is $O(N_t N_e^2)$ due to the global field computations at the predictor step. Note that the corrector step is still applicable even when the predictor step is accelerated using the PWTD algorithm [9]–[12] or the blocked FFT-based schemes [19]–[24]. Corrector updates cost only as much as the near-field computations of the acceleration schemes. iii) The corrector step (23) uses the averages of $\mathbf{T}(\mathbf{r}_i, t_n)$ and $\mathbf{T}(\mathbf{r}_i, t_{n-1})$ and $\mathbf{L}(\mathbf{r}_i, t_n)$ and $\mathbf{L}(\mathbf{r}_i, t_{n-1})$ (instead of $\mathbf{T}(\mathbf{r}_i, t_n)$ and $\mathbf{L}(\mathbf{r}_i, t_n)$, respectively) to update the solution estimated by the predictor step. This specific choice of averaging results in increased stability. Numerical experiments, which are presented in the next section, demonstrate that the stability and the accuracy of the scheme are superior to those of a similar TD-VIE solver that makes use of FIR to stabilize the solution [34]. Additionally, the proposed scheme is shown to be faster. iv) Unlike implementation of many implicit TDIE solvers, the implementation of the above scheme does not pre-compute nor store any discretized retarded field interactions before the time marching starts; as a result, it is memory efficient. The use of nodal spatial discretization schemes makes the computation of these discretized interactions fast; their repeated computation during marching does not increase the computation time drastically. Additionally, the MPI/OpenMP hybrid parallelization scheme described in [35], [36] is used to accelerate the time marching to enable the application of the proposed method to the analysis of wave interactions with electrically large and complex structures; further demonstrating the proposed method's stability even if the number of spatial discretization elements is considerably increased.

III. Numerical Results

In this section, the accuracy, stability, and applicability of the proposed TD-VIE solver are demonstrated via numerical experiments. In all examples considered here, the excitation is a

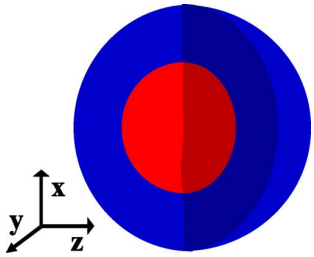

Fig. 1. Geometry of the layered dielectric microsphere.

plane wave, propagating in the z-direction with electric field $\mathbf{E}^{\rm inc}(\mathbf{r},t) = \hat{\mathbf{p}}\, E_0 G(t - z/c_b)$. Here, $E_0 = 1$ V/m is the electric field amplitude, $\hat{\mathbf{p}}$ is the polarization unit vector, and $G(t) = \cos[2\pi f_0(t-t_0)]\exp[-(t-t_0)^2/(2\varsigma^2)]$ is a modulated Gaussian pulse with modulation frequency f_0, bandwidth $f_{\rm bw}$, duration $\varsigma = 3/(2\pi f_{\rm bw})$, and delay $t_0 = 8\varsigma$. Whenever possible, the results obtained by the proposed TD-VIE solver are compared to those obtained analytically or by a similar TD-VIE solver, which makes use of the FIR to stabilize the solution [34]. In the remainder of the section, the proposed TD-VIE solvers with the predictor-corrector scheme and the FIR are abbreviated as TD-VIE-PC and TD-VIE-FIR, respectively.

A. Accuracy and Stability

To demonstrate its accuracy and stability, the proposed TD-VIE-PC is applied to the analysis of scattering from a (layered) dielectric microsphere. The microsphere resides in free space background and its center is located at the origin (Fig. 1). The inner and outer radii of the layer are $r_a = 0.25$ μm and $r_b = 0.5$ μm, respectively. The relative dielectric permittivities of the core and the layer are 1.5 and 1.75, respectively. The microsphere is excited with a plane wave with $\hat{\mathbf{p}} = \hat{\mathbf{x}}$, $f_0 = 0$ THz, and $f_{\rm bw} = 600$ THz; the maximum frequency of the excitation $f_{\max} = f_0 + f_{\rm bw}$. To quantify the accuracy of the TD-VIE-PC and compare it to that of the TD-VIE-FIR, relative energy error in frequency domain

$$err^{\rm sim}_{\Delta t,N_e}(\mathbf{r}_o) = \sqrt{\frac{\sum_{i=1}^{N_f}\left|\tilde{E}^{\rm scat,sim}_{x,\Delta t,N_e}(\mathbf{r}_o,f_i) - \tilde{E}^{\rm scat,mie}_{x}(\mathbf{r}_o,f_i)\right|^2}{\sum_{i=1}^{N_f}\left|\tilde{E}^{\rm scat,mie}_{x}(\mathbf{r}_o,f_i)\right|^2}}$$

is used. Here, $\tilde{E}^{\rm scat,sim}_{x,\Delta t,N_e}(\mathbf{r}_o,f_i)$ represents the x–component of the time harmonic scattered electric field at the observation point $\mathbf{r}_o$ and the frequency samples f_i, $i = 1,\ldots,N_f$, within the band $[f_0\ f_{\max}] = [0\ 600]$ THz, and is computed from

$$\tilde{E}^{\rm scat,sim}_{x,\Delta t,N_e}(\mathbf{r}_o,f) = \frac{\Im\{E^{\rm scat,sim}_{x,\Delta t,N_e}(\mathbf{r}_o,t)\}}{\Im\{G(t)\}}$$

where $\Im\{.\}$ represents the Fourier transform, $E^{\rm scat,sim}_{x,\Delta t,N_e}(\mathbf{r}_o,t)$ is the x–component of the time-domain scattered electric field computed at the observation point $\mathbf{r}_o$ by the TD-VIE-PC (sim $= \{\rm PC\}$) or the TD-VIE-FIR (sim $= \{\rm FIR\}$) for a given set of Δt and N_e. Here, $\tilde{E}^{\rm scat,mie}_{x}(\mathbf{r}_o,f_i)$ is computed using a Mie series code. For all computations of $err^{\rm sim}_{\Delta t,N_e}(\mathbf{r}_o)$, $\mathbf{r}_o = (0, 1.3\,\mu{\rm m}, 0)$ and $N_f = 48$. Note that this fixed location for $\mathbf{r}_o$ is outside the sphere, and thus $E^{\rm sim}_{x,\Delta t,N_e}(\mathbf{r}_o,t)$ is computed from the fields induced in the sphere as a post-processing step.

In the first set of simulations, the effect of spatial discretization on the accuracy of the TD-VIE-PC is characterized. Let j, $j = 1,\ldots,9$ represent the index of the simulation in this set; then Δd_j, $N_{e,j}$, $\Delta t_j = \Delta d_j/c_b$, and $\beta_j = 1/(2f_{\max}\Delta t_j)$ are the element size, the number of elements, the time step, and the over-sampling factor at simulation j, respectively. The largest and smallest element sizes are $\Delta d_1 = 0.06$ μm and $\Delta d_9 = 0.01$ μm; the corresponding number of element sizes are $N_{e,1} = 2469$ and $N_{e,9} = 523305$, respectively. For all nine simulations, the duration of simulation is fixed, $t \in [0\ 40]$ fs. Table I presents $err^{\rm sim}_{\Delta t_j,N_{e,j}}(\mathbf{r}_o)$, $j = 1,\ldots,9$, for sim $= \{\rm PC, FIR\}$. As expected, the accuracy increases ($err^{\rm sim}_{\Delta t_j,N_{e,j}}(\mathbf{r}_o)$, sim $= \{\rm PC, FIR\}$ decreases) with the increasing discretization density. While this trend is observed for both the TD-VIE-PC and TD-VIE-FIR, it should be noted that the TD-VIE-PC produces slightly more accurate results. More importantly, for the relatively denser discretizations, namely when $N_{e,j} \geq 132651$, solutions obtained from the TD-VIE-FIR are unstable while TD-VIE-PC maintains the stability of the solution for all nine simulations. The difference observed in the computational cost of TD-VIE-PC and TD-VIE-FIR is worthy of reporting. The CPU times needed to complete TDIE-VIE-FIR simulations are found to be at least 3.5 times greater than those needed to complete the TD-VIE-PC simulations. This is due to the repeated evaluation of previously calculated field values during time marching, which are needed for construction of the FIR in the form of a constant group delay [43]. In Fig. 2(a) and (b), $err^{\rm sim}_{\Delta t_j,N_{e,j}}(\mathbf{r}_o)$, sim $= \{\rm PC, FIR\}$ versus $N_{e,j}$ and Δt_j, $j = 1,\ldots,9$, are plotted, respectively.

For the sake of completeness, Fig. 3 compares $\tilde{E}^{\rm scat,PC}_{x,\Delta t_j,N_{e,j}}(\mathbf{r}_o,f)$, $j = 4$, and $\tilde{E}^{\rm scat,mie}_{x}(\mathbf{r}_o,f)$ in the frequency band of interest $[f_0\ f_{\max}]$. Note that for this simulation, $\Delta d_4 = 0.03$ μm, $N_{e,4} = 19381$, $\Delta t_4 = 0.10007$ fs, and $\beta_4 = 6.29$. As clearly seen from Fig. 3, these values of simulation parameters results in an accuracy level in the frequency band $[f_0\ f_{\max}]$, which is acceptable for most practical applications.

In the second set of simulations, the effect of increasing Δt beyond $\Delta d/c_b$, i.e., $\Delta t \geq \Delta d/c_b$, on the accuracy and the CPU time of the TD-VIE-PC simulations is characterized. In this set, $\Delta d = 0.02$ μm and $N_e = 65267$ are kept fixed for all eleven simulations, $j = 1,\ldots,11$, but the time step size is changed between $\Delta t_1 = \Delta d/c_b = 0.06671$ fs to $\Delta t_{11} = 1.5\Delta d/c_b = 0.10007$ fs; for those time step values, $\beta_1 = 9.44$ and $\beta_{11} = 6.29$, respectively. For all eleven simulations, the duration of simulation is fixed, $t \in [0\ 40$ fs$]$.Table II presents $err^{\rm PC}_{\Delta t_j,N_e}(\mathbf{r}_o), j = 1,\ldots,11$. Fig. 4 plots $err^{\rm PC}_{\Delta t_j,N_e}(\mathbf{r}_o)$ versus Δt_j, $j = 1,\ldots,11$;; where it is observed that the error decreases linearly with the time step size. This is expected since the method is first-order accurate in time discretization. Additionally, Table II presents the normalized CPU times needed for each simulation to be completed. This is also plotted in Fig. 4. As expected the CPU time increases linearly with the total number of time steps, i.e., $40/\Delta t_j$, as Δt_j decreases. One important conclusion drawn from the results of the second set of simulations is the fact that the time step can be pushed to $\sim$

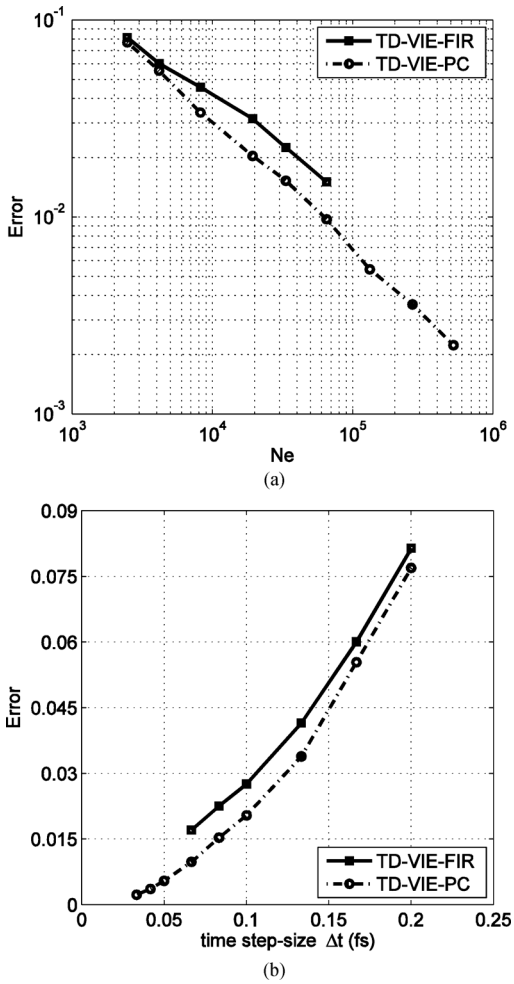

Fig. 2. $err^{\mathrm{sim}}_{\Delta t_j, N_{e,j}}(\mathbf{r}_o)$, sim $= \{\mathrm{PC}, \mathrm{FIR}\}$ versus (a) $N_{e,j}$ and (b) Δt_j, $j = 1, \ldots, 9$.

TABLE I
COMPARISON OF $err^{\mathrm{PC}}_{\Delta t, N_e}(\mathbf{r}_o)$ AND $err^{\mathrm{FIR}}_{\Delta t, N_e}(\mathbf{r}_o)$ FOR VARIOUS N_e AND Δt

$N_{e,j}$	Δd_j	Δt_j	β_j	$err^{\mathrm{PC}}_{\Delta t_j, N_{e,j}}(\mathbf{r}_o)$	$err^{\mathrm{FIR}}_{\Delta t_j, N_{e,j}}(\mathbf{r}_o)$
2469	0.0600	0.20014	3.14752	0.07690	0.08143
4169	0.0500	0.16678	3.77703	0.05538	0.06004
8217	0.0400	0.13343	4.72129	0.03386	0.04551
19381	0.0300	0.10007	6.29505	0.02040	0.03153
33401	0.0250	0.08339	7.55406	0.01527	0.02251
65267	0.0200	0.06671	9.44257	0.00974	0.01506
132651	0.0150	0.05003	12.59010	0.00542	unstable
267761	0.0125	0.04170	15.10812	0.00360	unstable
523305	0.0100	0.03336	18.88515	0.00223	unstable

$1.5\Delta d/c_b$ with no compromise on stability of the solution. This would not be possible without the predictor-corrector scheme.

The late-time stability of the TD-VIE-PC is investigated by increasing the duration of the simulation beyond 40 fs for the simulation with $\Delta d = 0.02$ μm, $N_e = 65267$, $\Delta t = \Delta d/c_b = 0.06671$ fs and $\beta = 9.44$. The simulation is continued until

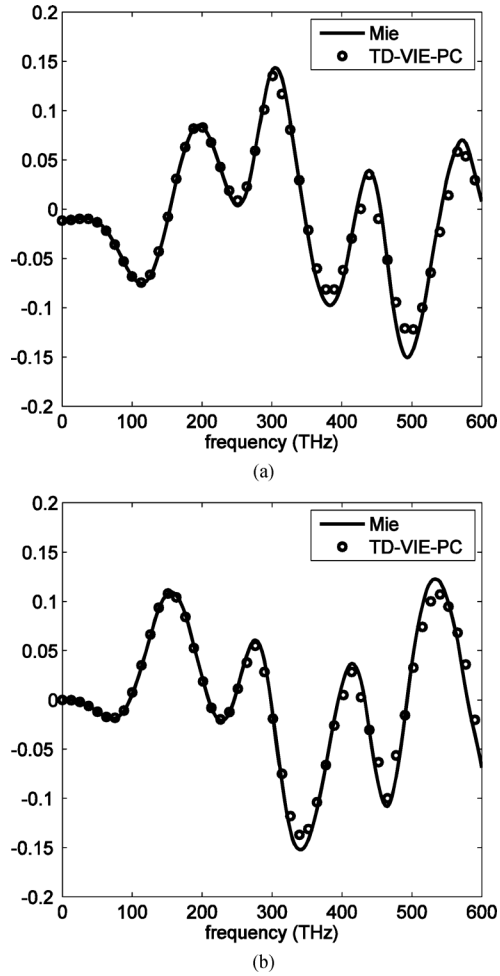

Fig. 3. Comparison of $\tilde{E}^{\mathrm{scat,PC}}_{x,\Delta t_j, N_{e,j}}(\mathbf{r}_o, f)$, $j = 4$, and $E^{\mathrm{scat,mie}}_x(\mathbf{r}_o, f)$ in the frequency band of interest $[f_0 \ f_{\max}]$. (a) Real part. (b) Imaginary part.

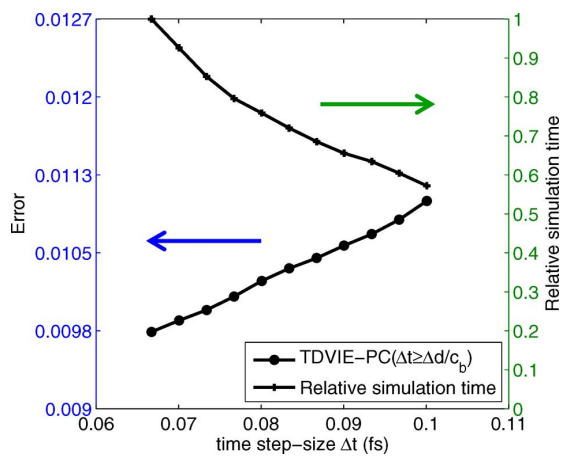

Fig. 4. $err^{\mathrm{PC}}_{\Delta t_j, N_e}(\mathbf{r}_o)$ and relative simulation time versus Δt_j, $j = 1, \ldots, 11$, for $N_e = 65267$.

the amplitude of the total electric field, $\mathbf{E}^{\mathrm{tot,PC}}_{\Delta t, N_e}(\mathbf{r}_o, t)$, is below 10^{-18}, which happens around $t = 100$ fs. Fig. 5(a) and (b) plot the x–component of the total electric field, $E^{\mathrm{tot,PC}}_x(\mathbf{r}_o, t)$ versus t and compares it to $E^{\mathrm{tot,mie}}_x(\mathbf{r}_o, t)$. Here, time domain total electric field $E^{\mathrm{tot,mie}}_x(\mathbf{r}_o, t)$ is obtained from

$$E^{\mathrm{tot,mie}}_x(\mathbf{r}_o, t) = \Im^{-1}[\tilde{E}^{\mathrm{tot,mie}}_x(\mathbf{r}_o, f)\Im\{G(t)\}]$$

TABLE II
$err^{\mathrm{PC}}_{\Delta t, N_e}(\mathbf{r}_o)$ AND RELATIVE SIMULATION TIME VERSUS. Δt ($N_e = 65267$)

Δt_j	β_j	$err^{\mathrm{PC}}_{\Delta_j, N_{e,j}}(\mathbf{r}_o)$	Relative simulation time
0.06671	9.44257	0.00974	1
0.07005	8.99293	0.00979	0.925995
0.07338	8.58416	0.00989	0.8526119
0.07672	8.21093	0.01008	0.7960199
0.08006	7.86881	0.01023	0.7587065
0.08339	7.55406	0.01038	0.7201493
0.08673	7.26352	0.01043	0.6853234
0.09006	6.99450	0.01057	0.6554726
0.09340	6.74470	0.01068	0.6343284
0.09673	6.51212	0.01079	0.6044776
0.10007	6.29505	0.01102	0.5721393

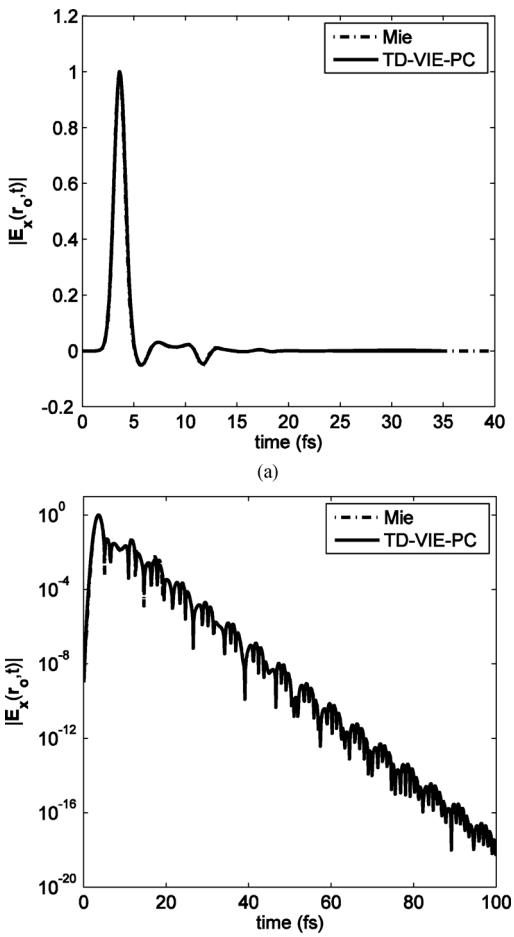

Fig. 5. Comparison of $E_x^{\mathrm{tot,PC}}(\mathbf{r}_o, t)$ for $N_e = 65267$, $\Delta t = \Delta d/c_b = 0.06671$ fs and $E_x^{\mathrm{tot,Mie}}(\mathbf{r}_o, t)$. (a) Linear scale. (b) Logarithmic scale.

where $\tilde{E}_x^{\mathrm{tot,mie}}(\mathbf{r}_o, f)$ is the time-harmonic total electric field computed using a Mie series code and $\Im^{-1}\{.\}$ represents inverse Fourier transform. The figures clearly show that the solution stays stable even after the amplitude of the field decreases below 10^{-18}.

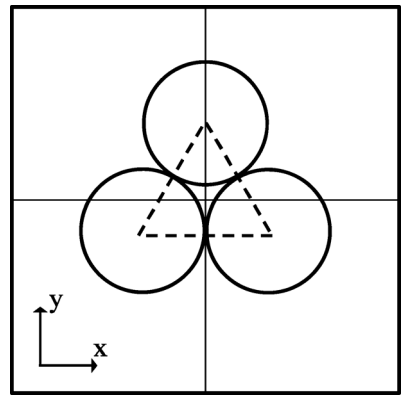

Fig. 6. Top view of the triangular ensemble of three dielectric microspheres. The center of the triangle connecting the centers of the spheres is located at the origin.

B. Practical Examples

To demonstrate its applicability, the proposed TD-VIE-PC is used in the characterization of transient electromagnetic waves on electrically large dielectric structures in two practical engineering scenarios.

1) Diffraction by Three Spheres: In this example, the backscattered diffraction patterns of a triangular ensemble of three homogeneous dielectric microspheres whose refractive indices are chosen to mimic that of a practical problem in life sciences microscopy [40] are calculated. The three spheres reside in a homogeneous background and the center of the triangle connecting the centers of the spheres is located at the origin (Fig. 6) [40]. The radius of each sphere is 0.5 μm and the relative dielectric permittivities of the spheres and the background medium are 2.35 and $\varepsilon_b = 2.1$, respectively. The ensemble of spheres is excited separately with two plane waves with i) $\hat{\mathbf{p}} = \hat{\mathbf{x}}$, $f_0 = 293$ THz, and $f_{\mathrm{bw}} = f_0/15$ THz and ii) $\hat{\mathbf{p}} = \hat{\mathbf{y}}$, $f_0 = 293$ THz, and $f_{\mathrm{bw}} = f_0/15$ THz. For both of the simulations, $\Delta d = 0.04$ μm and $N_e = 196235$; the simulations are carried out for $t \in [0\ 85]$ fs with $\Delta t = 0.13333$ fs. The scattered fields, $\mathbf{E}^{\mathrm{scat},1}(\mathbf{r}_o, t)$ and $\mathbf{E}^{\mathrm{scat},2}(\mathbf{r}_o, t)$ at $\mathbf{r}_o = (x, y, z)$, -6 μm $< y < 6$ μm, and $z = -2.048$ μm, are computed by the TD-VIE-PC under excitations (i) and (ii), respectively. Then, the time harmonic scattered fields $\tilde{\mathbf{E}}^{\mathrm{scat},1}(\mathbf{r}_o, f)$ and $\tilde{\mathbf{E}}^{\mathrm{scat},2}(\mathbf{r}_o, f)$ are computed from $\mathbf{E}^{\mathrm{scat},1}(\mathbf{r}_o, t)$ and $\mathbf{E}^{\mathrm{scat},2}(\mathbf{r}_o, t)$ respectively, using

$$\tilde{\mathbf{E}}^{\mathrm{scat},i}(\mathbf{r}_o, f) = \frac{\Im\{\mathbf{E}^{\mathrm{scat},i}(\mathbf{r}_o, t)\}}{\Im\{G(t)\}},\ i = 1, \ldots, 2$$

at $f = 293$ THz. Fig. 7(a) and (b) plot distributions of normalized scattered field intensities, which are computed using

$$\tilde{I}^{\mathrm{scat},i}(\mathbf{r}_o, f) = \frac{\left|\tilde{\mathbf{E}}^{\mathrm{scat},i}(\mathbf{r}_o, f)\right|^2}{\max\left|\tilde{\mathbf{E}}^{\mathrm{scat},i}(\mathbf{r}_o, f)\right|^2},\ i = 1, \ldots, 2,$$

respectively. The normalized intensity profiles agree very well with those reported in [40].

2) Sub-Wavelength Thin Film Detection Using PNJ: A photonic nanojet (PNJ) [41] is a narrow high intensity light beam

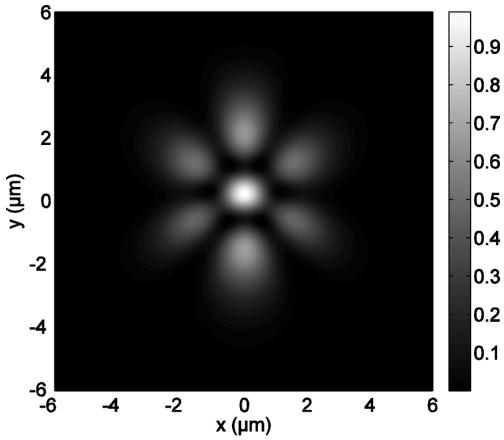

(a)

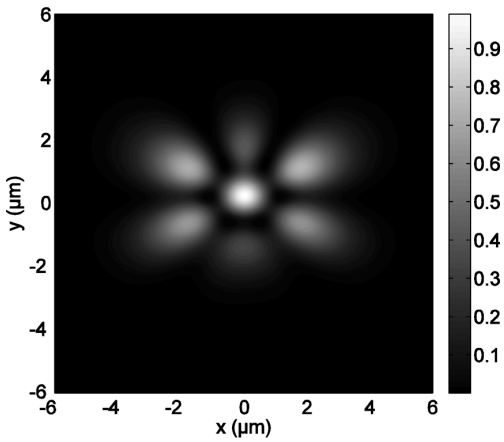

(b)

Fig. 7. Normalized intensity of the scattered field, $\tilde{I}^{\mathrm{scat},i}(\mathbf{r}_o, f)$ at $\mathbf{r}_o = (x, y, z)$, $-6\ \mu\mathrm{m} < x < 6\ \mu\mathrm{m}$, $-6\ \mu\mathrm{m} < y < 6\ \mu\mathrm{m}$, and $z = -2.048\ \mu\mathrm{m}$, and $f = 293$ THz under the excitation of (a) $\hat{\mathbf{x}}$–polarized ($i = 1$) and (b) $\hat{\mathbf{y}}$– polarized plane wave ($i = 2$).

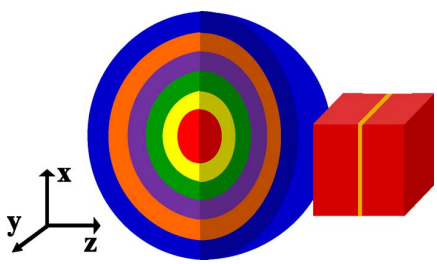

Fig. 8. Geometry of the dielectric microsphere with five equally spaced concentric spherical layers and the thin film embedded at the midpoint of a dielectric cube.

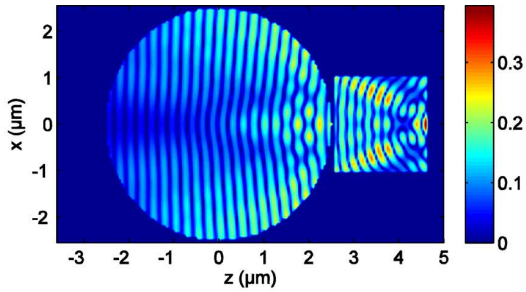

(a)

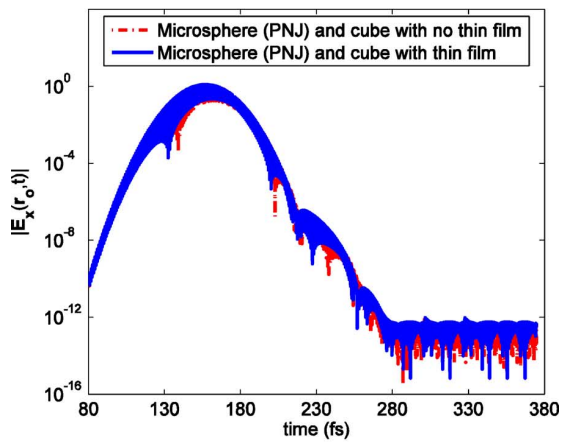

(b)

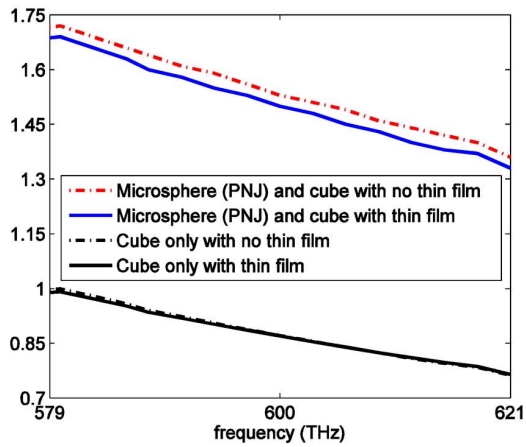

(c)

Fig. 9. (a) Absolute value of the total electric field distribution along the central cross section (on the xz–plane at $y = 0$) at time $t = 200$ fs for scenario (ii). (b) $|E_x^{\mathrm{tot},1}(\mathbf{r}_o, t)|$ and $|E_x^{\mathrm{tot},2}(\mathbf{r}_o, t)|$ computed at the origin $\mathbf{r}_o = (0, 0, 0)$ for scenarios (i) and (ii). (c) Comparison of $\left|\tilde{E}_x^{\mathrm{scat},i}(\mathbf{r}_o, f)\right|$, $i = 1, \ldots, 4$, computed at $\mathbf{r}_o = (0, 0, 4.75\ \mu\mathrm{m})$ within band [579 621] THz for scenarios (i), (ii), (iii), and (iv).

that emerges from the shadow-side surface of a multilayered dielectric microsphere, illuminated by plane-wave. PNJ can be of practical use in the detection of sub-wavelength dielectric features, examples of which include natural or engineered nanoparticles. The operation of a PNJ in such a scenario has been numerically demonstrated in [42].

Here, a dielectric microsphere with five equally spaced concentric spherical layers is used to generate a PNJ. The microsphere resides in a free space background and its center is located at the origin. The radius of the core (inner most sphere) is 0.416 μm and the thickness of each layer is 0.416 μm [42] (Fig. 8). The relative dielectric permittivities of the layers and the core (listed in order from outer to inner) are 1.02, 1.04, 1.06, 1.08, 1.10, and 1.12, respectively. The microsphere is used to generate a PNJ that is used in the detection of a 50 nm thin film embedded at the midpoint of a dielectric cube with side length 2.0 μm (Fig. 8). The relative dielectric permittivities of the thin film and the cube are 1.96 and 1.69, respectively. To investigate if the PNJ generated by the microsphere can create a scattered field that can be used in the detection of the thin film, four scenarios are considered: i) Microsphere and cube are present but thin film is removed. ii) Microsphere, cube, and

thin film are all present. iii) Only cube is present, microsphere and thin film are removed. iv) Cube and thin film are present but the microsphere is removed. In all four scenarios, the excitation is a plane wave with $\hat{\mathbf{p}} = \hat{\mathbf{x}}$, $f_0 = 600$ THz, and $f_{\rm bw} = 30$ THz, and all the simulations are carried out for 380 fs with $\Delta t = 0.16667$ fs. For all four scenarios, $\Delta d = 0.05$ μm, which results in $N_e = \{592226, 592226, 560226, 560226\}$ discretization elements, respectively. Fig. 9(a) visualizes, for the scenario (ii), the absolute value of the total electric field distribution along the central cross section (on the xz – plane at $y = 0$) at a fixed moment in time $t = 200$ fs. Fig. 9(b) plots the absolute value of the x–component of the total fields, $\left|E_x^{\rm tot,1}(\mathbf{r}_o, t)\right|$ and $\left|E_x^{\rm tot,2}(\mathbf{r}_o, t)\right|$, at the origin $\mathbf{r}_o = (0, 0, 0)$, computed by the TD-VIE-PC for scenarios i) and ii). This figure clearly shows that the solution stays stable. Next, the scattered fields $E_x^{{\rm scat},i}(\mathbf{r}_o, t)$, at $\mathbf{r}_o = (0,\ 0,\ 4.75\ \mu{\rm m})$, $i = 1, \ldots, 4$, are computed by the TD-VIE-PC for all four scenarios. Then, the time harmonic scattered fields $\tilde{E}_x^{{\rm scat},i}(\mathbf{r}_o, f)$ are computed from $E_x^{{\rm scat},i}(\mathbf{r}_o, f)$ using

$$\tilde{E}_x^{{\rm scat},i}(\mathbf{r}_o, f) = \frac{\Im\{E_x^{{\rm scat},i}(\mathbf{r}_o, t)\}}{\Im\{G(t)\}},\ i = 1, \ldots, 4$$

within the frequency band $[f_0 f_{\max}] = [579\ 621]$ THz. Fig. 9(c) compares $\left|\tilde{E}_x^{{\rm scat},i}(\mathbf{r}_o, f)\right|$, $i = 1, \ldots, 4$. As clearly shown in the figure the shift observed between $\left|\tilde{E}_x^{{\rm scat},1}(\mathbf{r}_o, f)\right|$ and $\left|\tilde{E}_x^{{\rm scat},2}(\mathbf{r}_o, f)\right|$ is larger than shift between $\left|\tilde{E}_x^{{\rm scat},3}(\mathbf{r}_o, f)\right|$ and $\left|\tilde{E}_x^{{\rm scat},4}(\mathbf{r}_o, f)\right|$; this indicates that the high intensity PNJ generated by the microsphere increases the sensitivity of the scattered field and provides a mechanism for detecting the presence of the thin film.

IV. Conclusion

An explicit and stable MOT scheme for solving the TD-VIE to analyze transient electromagnetic wave interactions on inhomogeneous dielectric structures is presented. The method achieves its stability, while maintaining its explicitness, by employing a predictor-corrector scheme at each time step. The proposed MOT scheme is demonstrated to be far superior in stability and computational cost when compared to the existing explicit schemes that make use of filtering techniques to stabilize the solution. Furthermore, numerical results presented in this work demonstrate the proposed method to maintain its stability even when applied to the analysis of electromagnetic wave interactions with electrically large structures meshed using approximately half a million discretization elements.

Future work includes generalizing the scheme to allow for the analysis of transient wave interactions on scatterers with non-linear and dispersive material properties. Moreover, the development of adaptive time stepping techniques and incorporation of accelerations schemes are underway.

Appendix

To approximate the second-order time derivative the following finite difference schemes are used.

Central difference (CD) scheme:

$$\partial_t^2 \mathbf{F}(\mathbf{r}, t)\big|_{\mathbf{r}=\mathbf{r}_i, t=t_n} \approx \frac{\mathbf{F}(\mathbf{r}_i, t_{n+1}) - 2\mathbf{F}(\mathbf{r}_i, t_n) + \mathbf{F}(\mathbf{r}_i, t_{n-1})}{\Delta t^2}. \tag{A1}$$

Backward difference (BD) scheme:

$$\partial_t^2 \mathbf{F}(\mathbf{r}, t)\big|_{\mathbf{r}=\mathbf{r}_i, t=t_n} \approx \frac{\mathbf{F}(\mathbf{r}_i, t_n) - 2\mathbf{F}(\mathbf{r}_i, t_{n-1}) + \mathbf{F}(\mathbf{r}_i, t_{n-2})}{\Delta t^2}. \tag{A2}$$

To approximate the second-order space derivative, a CD scheme is used as described in the following:

$$\nabla\nabla\cdot\mathbf{F}(\mathbf{r}, t) = [\,\hat{\mathbf{x}} \quad \hat{\mathbf{y}} \quad \hat{\mathbf{z}}\,] \begin{bmatrix} \partial_x^2 & \partial_x\partial_y & \partial_x\partial_z \\ \partial_y\partial_x & \partial_y^2 & \partial_y\partial_z \\ \partial_z\partial_x & \partial_z\partial_y & \partial_z^2 \end{bmatrix} \begin{bmatrix} F_x(\mathbf{r}, t) \\ F_y(\mathbf{r}, t) \\ F_z(\mathbf{r}, t) \end{bmatrix} \tag{A3}$$

where $\mathbf{F}(\mathbf{r}, t) = \hat{\mathbf{x}}\, F_x(\mathbf{r}, t) + \hat{\mathbf{y}}\, F_y(\mathbf{r}, t) + \hat{\mathbf{z}}\, F_z(\mathbf{r}, t)$. Each entry of the matrix in (A3) is discretized using a CD scheme. For an un-mixed second order derivative in (A3):

$$\partial_z^2 F_z(\mathbf{r}, t)\big|_{\mathbf{r}=\mathbf{r}_i, t=t_n} \approx \frac{F_z(\mathbf{r}_k, t_n) - 2F_z(\mathbf{r}_i, t_n) + F_z(\mathbf{r}_m, t_n)}{\Delta d^2}. \tag{A4}$$

Here, sample indices k and m are chosen such at $x_k = x_i$, $y_k = y_i$, $z_k = z_i + \Delta d$ and $x_m = x_i$, $y_m = y_i$, $z_m = z_i - \Delta d$. For a mixed second-order derivative in (A3):

$$\partial_x\partial_y F_y(\mathbf{r}, t)\big|_{\mathbf{r}=\mathbf{r}_i, t=t_n} \approx \frac{F_y(\mathbf{r}_k, t_n) - F_y(\mathbf{r}_m, t_n) + F_y(\mathbf{r}_l, t_n) - F_y(\mathbf{r}_j, t_n)}{4\Delta d^2}. \tag{A5}$$

Here, sample indices k, m, l, and j are chosen such that $x_k = x_i + \Delta d$, $y_k = y_i + \Delta d$, $z_k = z_i$; $x_m = x_i + \Delta d$, $y_m = y_i - \Delta d$, $z_m = z_i$; $x_l = x_i - \Delta d$, $y_l = y_i + \Delta d$, $z_l = z_i$; and $x_j = x_i - \Delta d$, $y_j = y_i - \Delta d$, $z_j = z_i$. Other derivatives in (A3) are approximated similarly. Then, one can symbolically write

$$\nabla\nabla\cdot\mathbf{F}(\mathbf{r}, t)\big|_{\mathbf{r}=\mathbf{r}_i, t=t_n} \approx \bar{\mathbf{G}}_i \cdot \{\forall \mathbf{F}(\mathbf{r}_s, t_n) : |\mathbf{r}_s - \mathbf{r}_i| = \Delta d, \mathbf{r}_s = \mathbf{r}_i\} \tag{A6}$$

where $\bar{\mathbf{G}}_i$ is a matrix that chooses the components of the samples at $\mathbf{r}_s$, which are neighboring $\mathbf{r}_i$, and multiplies them with the correct coefficients to produce the CD approximation.

Acknowledgment

The authors would like to thank the King Abdullah University of Science and Technology Supercomputing Laboratory for providing the required computational resources. The Mie series results, which are used as reference, are obtained from a Mie series code that has been developed by M. Furqan. The authors would also like to thank Dr. M. Taskinen and Dr. H. A. Ülkü for the fruitful discussions over the singularity extraction technique and its implementation, respectively.

References

[1] S. M. Rao and D. R. Wilton, "Transient scattering by conducting surfaces of arbitrary shape," *IEEE Trans. Antennas Propag.*, vol. 39, no. 1, pp. 56–61, Jan. 1991.

[2] S. Dodson, S. P. Walker, and M. J. Bluck, "Implicitness and stability of time domain integral equation scattering analysis," *ACES J.*, vol. 13, no. 3, pp. 291–301, Nov. 1998.

[3] D. A. Vechinski and S. M. Rao, "A stable procedure to calculate the transient scattering by conducting surfaces of arbitrary shape," *IEEE Trans. Antennas Propag.*, vol. 40, no. 6, pp. 661–665, Jun. 1992.

[4] S. M. Rao and T. K. Sarkar, "Numerical solution of time-domain integral equations for arbitrarily conductor/dielectric composite bodies," *IEEE Trans. Antennas Propag.*, vol. 50, no. 12, pp. 1831–1837, Dec. 2002.

[5] B. P. Rynne and P. D. Smith, "Stability of time marching algorithms for the electric field integral equation," *J. Electromagn. Waves Appl.*, vol. 4, no. 12, pp. 1181–1205, 1990.

[6] A. Sadigh and E. Arvas, "Treating the instabilities in marching-on-in-time method from a different perspective," *IEEE Trans. Antennas Propag.*, vol. 41, no. 12, pp. 1695–1702, Dec. 1993.

[7] P. J. Davies, "A stability analysis of a time marching scheme for the general surface electric field integral equation," *Appl. Num. Math.*, vol. 27, no. 1, pp. 33–57, May 1998.

[8] G. Manara, A. Monorchio, and R. Reggiannini, "A space-time discretization criterion for a stable time-marching solution of the electric field integral equation," *IEEE Trans. Antennas Propag.*, vol. 45, no. 3, pp. 527–532, Mar. 1997.

[9] N. T. Gres, A. A. Ergin, E. Michielssen, and B. Shanker, "Volume-integral-equation-based analysis of transient electromagnetic scattering from three-dimensional inhomogeneous dielectric objects," *Radio Sci.*, vol. 36, no. 3, pp. 379–386, May/Jun. 2001.

[10] B. Shanker, K. Aygun, and E. Michielssen, "Fast analysis of transient scattering from lossy inhomogeneous dielectric bodies," *Radio Sci.*, vol. 39, no. 2, Mar. 2004.

[11] B. Shanker, A. A. Ergin, M. Lu, and E. Michielssen, "Fast analysis of transient electromagnetic scattering phenomena using the multilevel plane wave time domain algorithm," *IEEE Trans. Antennas Propag.*, vol. 51, no. 3, pp. 628–641, Mar. 2003.

[12] A. A. Ergin, B. Shanker, and E. Michielssen, "The plane-wave time-domain algorithm for the fast analysis of transient wave phenomena," *IEEE Antennas Propag. Mag.*, vol. 41, no. 4, pp. 39–52, Sep. 1999.

[13] B. Shanker, M. Lu, J. Yuan, and E. Michielssen, "Time domain integral equation analysis of scattering from composite bodies via exact evaluation of radiation fields," *IEEE Trans. Antennas Propag.*, vol. 57, no. 5, pp. 1506–1520, May 2009.

[14] Y. Shi, M. Xia, R. Chen, E. Michielssen, and M. Lu, "Stable electric field TDIE solvers via quasi-exact evaluation of MOT matrix elements," *IEEE Trans. Antennas Propag.*, vol. 59, no. 2, pp. 574–585, Feb. 2011.

[15] H. A. Ulku and A. A. Ergin, "Analytical evaluation of transient magnetic fields due to RWG current bases," *IEEE Trans. Antennas Propag.*, vol. 55, no. 12, pp. 3565–3575, Dec. 2007.

[16] H. A. Ulku and A. A. Ergin, "Application of analytical retarded-time potential expressions to the solution of time domain integral equations," *IEEE Trans. Antennas Propag.*, vol. 59, no. 11, pp. 4123–4131, Nov. 2011.

[17] D. S. Weile, G. Pisharody, N.-W. Chen, B. Shanker, and E. Michielssen, "A novel scheme for the solution of the time-domain integral equations of electromagnetics," *IEEE Trans. Antennas Propag.*, vol. 52, no. 1, pp. 283–295, Jan. 2004.

[18] R. A. Wildman, G. Pisharody, D. S. Weile, B. Shanker, and E. Michielssen, "An accurate scheme for the solution of the time-domain integral equations of electromagnetics using higher order vector bases and band-limited extrapolation," *IEEE Trans. Antennas Propag.*, vol. 52, no. 11, pp. 2973–2984, Nov. 2004.

[19] A. E. Yilmaz, J. M. Jin, and E. Michielssen, "Time domain adaptive integral method for surface integral equations," *IEEE Trans. Antennas Propag.*, vol. 52, no. 3, pp. 2692–2708, Oct. 2004.

[20] A. E. Yilmaz, D. S. Weile, B. Shanker, J. M. Jin, and E. Michielssen, "Fast analysis of transient scattering in lossy media," *IEEE Antennas Wireless Propag. Lett.*, vol. 1, no. 1, pp. 14–17, 2002.

[21] A. E. Yilmaz, J. M. Jin, and E. Michielssen, "Analysis of low-frequency electromagnetic transients by an extended time-domain adaptive integral method," *IEEE Trans. Adv. Packag.*, vol. 30, no. 2, pp. 301–312, May 2007.

[22] H. Bagci, A. E. Yilmaz, V. Lomakin, and E. Michielssen, "Fast solution of mixed-potential time-domain integral equations for half-space environments," *IEEE Trans. Geosci. Remote Sensing*, vol. 43, no. 2, pp. 269–279, Feb. 2005.

[23] H. Bagci, A. E. Yilmaz, J.-M. Jin, and E. Michielssen, "Fast and rigorous analysis of EMC/EMI phenomena on electrically large and complex cable-loaded structures," *IEEE Trans. Electromagn. Comp.*, vol. 49, no. 2, pp. 361–381, May 2007.

[24] H. Bagci, A. E. Yilmaz, and E. Michielssen, "An FFT-accelerated time-domain multiconductor transmission line simulator," *IEEE Trans. Electromagn. Comp.*, vol. 52, no. 1, pp. 199–214, Feb. 2010.

[25] H. Bagci, F. P. Andriulli, F. Vipiana, G. Vecchi, and E. Michielssen, "A well-conditioned integral-equation formulation for efficient transient analysis of electrically small microelectronic devices," *IEEE Trans. Adv. Packag.*, vol. 33, no. 2, pp. 468–480, May 2010.

[26] F. P. Andriulli, H. Bagci, F. Vipiana, G. Vecchi, and E. Michielssen, "A marching-on-in-time hierarchical scheme for the time domain electric field integral equation," *IEEE Trans. Antennas Propag.*, vol. 55, no. 12, pp. 3734–3738, Dec. 2007.

[27] F. P. Andriulli, H. Bagci, F. Vipiana, G. Vecchi, and E. Michielssen, "Analysis and regularization of the TD-EFIE low-frequency breakdown," *IEEE Trans. Antennas Propag.*, vol. 57, no. 7, pp. 2034-2–46, Jul. 2009.

[28] A. G. Nerukh, I. V. Scherbatko, and M. Marciniak, *Electromagnetics of Modulated Media with Applications to Photonics*. Warsaw, Poland: Nat. Inst. Telecom., 2001.

[29] F. V. Fedotov, A. G. Nerukh, T. M. Benson, and P. Sewell, "Investigation of electromagnetic field in a layer with time-varying medium by Volterra integral equation method," *J. Lightw. Technol.*, vol. 21, no. 1, pp. 305–314, Jan. 2003.

[30] A. Al-Jarro, P. Sewell, T. M. Benson, and A. Nerukh, "Effective and flexible analysis for propagation in time varying waveguides," *Opt. Quantum Electron.*, vol. 36, pp. 133–144, 2004.

[31] T. M. Benson, A. Al-Jarro, P. Sewell, V. Janyani, J. D. Paul, and A. Vukovic, "Simulation of nonlinear integrated photonics devices: A comparison of TLM and numerical time domain integral equation approach," in *Ultra-Wideband, Short-Pulse Electromagnetics*, F. Sabath, E. L. Mokole, U. Schenk, and D. Nitsch, Eds. New York: Springer, 2007, vol. 7, pp. 80–88.

[32] A. Al-Jarro, P. Sewell, T. M. Benson, and A. Vukovic, "A Volterra integral equation algorithm on triangulated space time meshes," in *Proc. Workshop on Computational Electromagnetics in Time-Domain*, Perugia, 2007.

[33] A. Al-Jarro, P. Sewell, T. M. Benson, and A. Vukovic, "A Volterra time-domain integral equation algorithm on unstructured meshes: 3D model," in *Proc. ACES Symp.*, Monterey, 2009, pp. 792–796.

[34] A. Al-Jarro, P. Sewell, T. M. Benson, A. Vukovic, and J. Paul, "Transient time-dependent electric field of dielectric bodies using the Volterra integral equation in three-dimensions," *Progress Electromagn. Res.*, vol. 110, pp. 179–197, 2010.

[35] A. Al-Jarro and H. Bagci, "A hybrid MPI/OpenMP parallelization scheme for explicit solution of the Volterra integral equation," in *Proc. Comput. Electromagn. Int. Workshop (CEM)*, Izmir, 2011, pp. 128–131.

[36] A. Al-Jarro, M. Cheeseman, and H. Bagci, "Distributed-memory parallelization of an explicit time-domain volume integral equation solver on Blue Gene/P," *Appl. Comput. Electromagn. Soc. (ACES) J.*, vol. 27, no. 2, pp. 132–144, 2012.

[37] R. Courant, K. Friedrichs, and H. Lewy, "On the partial difference equations of mathematical physics," *IBM J.*, vol. 11, pp. 215–234, 1967.

[38] C. D. Sarris, *Adaptive Mesh Refinement for Time-Domain Numerical Electromagnetics*. San Rafael, CA: Morgan and Claypool, 2006.

[39] N. Godel, S. Schomann, T. Warburton, and M. Clemens, "GPU accelerated Adams–Bashforth multirate discontinuous Galerkin FEM simulation of high-frequency electromagnetic fields," *IEEE Trans. Magn.*, vol. 46, no. 8, pp. 2735–2738, Aug. 2010.

[40] R. L. Coe and E. J. Seibel, "Improved near-field calculations using vectorial diffraction integrals in the finite-difference time-domain method," *J. Opt. Soc. Am. A.*, vol. 28, no. 8, pp. 1776–1783, Aug. 2011.

[41] S.-C. Kong, A. Taflove, and V. Backman, "Quasi one-dimensional light beam generated by a graded-index microsphere," *Opt. Express*, vol. 17, no. 5, pp. 3722–3731, 2009.

[42] C. M. Ruiz and J. J. Simpson, "Detection of embedded ultra-subwavelength-thin dielectric features using elongated photonic nanojets," *Opt. Express*, vol. 18, no. 16, pp. 16805–16812, 2010.

[43] A. V. Oppenheim, *Discrete-Time Signal Processing*. Englewood Cliffs, NJ: Prentice-Hall, 1989.

[44] J. Waldvogel, "The Newtonian potential of homogeneous cube," *J. Appl. Math. Phys.*, vol. 27, no. 6, pp. 388–398, 1979.
[45] R. D. Graglia, "On the numerical integration of the linear shape functions times the 3-D Green's function or its gradient on a plane triangle," *IEEE Trans. Antennas Propag.*, vol. 41, no. 10, pp. 1448–1455, Oct. 1993.
[46] A. Taflove and S. C. Hagness, *Computational Electrodynamics: The Finite-Difference Time-Domain Method*. Boston, MA: Artech House.

Ahmed Al-Jarro (M'11) received the B.Eng. degree in electronic engineering with Spanish and the Ph.D. degree in electrical and electronic engineering from the University of Nottingham, Nottingham, U.K., in 2001 and 2004, respectively.

From 2004 to 2010, he was a Research Assistant and Research Fellow at the George Green Institute for Electromagnetics Research (GGIEMR), University of Nottingham. In 2011, he joined the Division of Physical Sciences and Engineering at King Abdullah University of Science and Technology (KAUST), Thuwal, Saudi Arabia, as a Postdoctoral Research Fellow. His research interests are in the field of computational electromagnetics for the analysis of photonic and optical devices. He is currently working on the development of explicit and stable marching-on-in-time based schemes for solving the time domain volume integral equation, and their efficient parallelization.

Dr. Al-Jarro was the recipient of the EPSRC Knowledge Transfer Secondment in collaboration with Photon Design Ltd., Oxford, U.K., from the University of Nottingham Research Innovation Services, UK, in 2010. He was also the recipient of the Japan Society for the Promotion of Science, JSPS, Fellowship Award in 2010.

Mohamed A. Salem (M'09) received the B.Sc., M.Sc., and Ph.D. degrees in electronic and telecommunications engineering from Ain Shams University, Cairo, Egypt, and the Ph.D. degree in electrical engineering from New Jersey Institute of Technology (NJIT), Newark, NJ, in 2001, 2004, 2008, and 2009, respectively.

Since 2010, he has been with the Computational Electromagnetics Laboratory, King Abdullah University of Science and Technology (KAUST), Thuwal, Saudi Arabia, as a Postdoctoral Fellow where he is working on analytic and computational aspects of wave propagation and scattering problems. His research interests include the mathematical and numerical modeling of wave propagation and scattering phenomena, electromagnetic field theory, and computational frequency- and time-domain methods for numerical simulation of wave propagation and scattering processes.

Hakan Bağcı (M'06) received the B.Sc. degree in electrical and electronics engineering from Bilkent University, Ankara, Turkey, in 2001 and the M.Sc. and Ph.D. degrees in Electrical and Computer Engineering from the University of Illinois at Urbana-Champaign (UIUC), Urbana, in 2003 and 2007, respectively.

From June 1999 to July 2001, he worked as an Undergraduate Researcher at the Computational Electromagnetics Group, Bilkent University. From 2001 to 2007, he was a Research Assistant at the Center for Computational Electromagnetics and Electromagnetics Laboratory, UIUC. From 2007 to 2009, he worked as a Research Fellow at the Radiation Laboratory, University of Michigan. In 2009, he joined the Division of Physical Sciences and Engineering at the King Abdullah University of Science and Technology (KAUST), Thuwal, Saudi Arabia, as an Assistant Professor. His research interests include various aspects of computational electromagnetics with emphasis on time-domain integral equations and their fast marching-on-in-time based solutions, well-conditioned integral-equation formulations, and development of fast hybrid methods for analyzing statistical EMC/EMI phenomena on complex and fully loaded platforms.

Dr. Bağcı was the recipient of the 2008 International Union of Radio Scientists (URSI) Young Scientist Award and the 2004–2005 Interdisciplinary Graduate Fellowship from the Computational Science and Engineering Department, UIUC. His paper titled "Fast and rigorous analysis of EMC/EMI phenomena on electrically large and complex structures loaded with coaxial cables" was one of the three finalists (with honorable mention) for the 2008 Richard B. Schulz Best Transactions Paper Award given by the IEEE Electromagnetic Compatibility Society. He authored and coauthored three finalist papers and another paper, which is awarded honorable mention, in the student paper competitions at the 2005, 2008, and 2010, IEEE Antennas and Propagation Society International Symposiums.

Trevor M. Benson (M'95–SM'01) received a First Class honors degree in physics and the Clark Prize in experimental physics and the Ph.D. degree in electronic and electrical engineering from the University of Sheffield, Sheffield, U.K., in 1979 and 1982, respectively, and the D.Sc. degree from the University of Nottingham, Nottingham, U.K., in 2005.

After spending over six years as a Lecturer at University College Cardiff, he moved to The University of Nottingham in 1989. He was promoted to a Chair in Optoelectronics in 1996, having previously been Senior Lecturer (1989) and Reader (1994). Since October 2011, he has been Director of the George Green Institute for Electromagnetics Research at The University of Nottingham. His research interests include experimental and numerical studies of electromagnetic fields and waves with particular emphasis on the theory, modeling and simulation of optical waveguides, lasers and amplifiers, nano-scale photonic circuits and electromagnetic compatibility.

Prof. Benson is a Fellow of the Institute of Engineering Technology (FIET) and the Institute of Physics (FInst.P). He was elected a Fellow of the Royal Academy of Engineering in 2005 for his achievements in the development of versatile design software used to analyze propagation in optoelectronic waveguides and photonic integrated circuits.

Phillip Sewell (M'89–SM'04) was born in London, U.K., in 1965. He received the B.Sc. degree in electrical and electronic engineering with first class honors and the Ph.D. degree from the University of Bath, Bath, U.K., in 1988 and 1991, respectively.

From 1991 to 1993, he was a Post-Doctoral Fellow at the University of Ancona, Ancona, Italy. In 1993, he was appointed as a Lecturer in the School of Electrical and Electronic Engineering, University of Nottingham, Nottingham, U.K. In 2001 and 2005, he was promoted to Reader and Professor of Electromagnetics at the same university. His research interests involve analytical and numerical modeling of electromagnetic problems, with application to optoelectronics, microwaves, and electrical machines.

Ana Vukovic (M'97) was born in Nis, Yugoslavia, in 1968. She received the Diploma of Engineering degree in electronics and telecommunication from the University of Nis, Nis, Yugoslavia, in 1992, and the Ph.D. degree from the University of Nottingham, Nottingham, U.K., in 2000.

From 1999 to 2001, she was a Research Associate with the University of Nottingham. In 2001, she joined the School of Electrical and Electronic Engineering, University of Nottingham, as a Lecturer. In 2008, she became an Associate Professor with the University of Nottingham. Her research interests are in the area of electromagnetics with a particular emphasis on applications in optoelectronics and microwaves.